A Quasigeostrophic Model for Moist Storm Tracks

ALEXANDRE LAÎNÉ AND GUILLAUME LAPEYRE

LMD/IPSL, ENS/CNRS, Paris, France

GWENDAL RIVIÈRE

CNRM/GAME, Météo-France/CNRS, Toulouse, France

(Manuscript received 30 July 2010, in final form 24 November 2010)

ABSTRACT

The effect of moisture and latent heat release is investigated in the context of a three-level quasigeostrophic model on the sphere. The model is based on an existing dry model that was shown to be able to reproduce the midlatitude synoptic and low-frequency variability of the troposphere. In addition to potential vorticity equations, moisture evolution equations are included with a simple precipitation scheme. The model can be forced using reanalysis datasets to represent the observed climatology.

After the description of the model, the Northern Hemisphere midlatitude climatic characteristics of the moist model are compared to its dry counterpart and to the 40-yr ECMWF Re-Analysis (ERA-40). The jet of the moist model is weakened in its central and northern part and enhanced in its southern part compared to the dry version, which generally decreases the model biases compared to reanalyses. Latent heating processes are mainly responsible for the global decrease in westerlies in the jet-core regions. Precipitation mainly occurs slightly poleward of the jet axes, thereby reducing the meridional temperature gradient and the wind through thermal wind balance. The mean synoptic activity is reduced according to the decrease in baroclinicity, as well as the mean low-frequency variability. A diagnosis of synoptic wave breaking is performed and the characteristics of the moist model are closer to the ones found in reanalyses, especially with more occurrence of cyclonic wave breaking. Weather regimes are slightly better represented in the moist model, although changes are weak compared to the intrinsic model biases. The behavior of the moist model around its climatology indicates that it could be used to run sensitivity experiments.

1. Introduction

Understanding what affects the dynamics of midlatitude storm tracks and their relation with the low-frequency variability of the atmosphere has led to numerous studies in the past (e.g., Lau 1988; Hoskins and Valdes 1990; Chang et al. 2002). Synoptic-scale atmospheric perturbations (i.e., with periods from 2 to 6 days) are produced through barotropic and baroclinic instabilities of the jet stream. They can extract energy from the large-scale flow due to these instabilities and give back to it when they decay at the storm-track exit (Chang and Orlanski 1993). The interactions between the jet stream and atmospheric disturbances give rise to the atmospheric variability (Branstator 1995). In particular, there exist intrinsic modes of variability, called weather regimes, which are maintained in time (Vautard and Legras 1988). In this context, Marshall and Molteni (1993, hereafter MM93) have developed a three-layer dry model in spherical geometry (hereafter the MM93 model) based on the quasigeostrophic (QG) equations of fluid motion. The model shows interesting properties in terms of high- and low-frequency variability in midlatitudes, similar to the observed ones (MM93; D'Andrea and Vautard 2001). This model therefore served as a basis for analyses of the midlatitudes (e.g., Corti et al. 1997; D'Andrea and Vautard 2001; Rivière 2009).

Most of the studies of the atmospheric storm track have examined its behavior in a dry context, but several authors (e.g., Chang et al. 2002; Hoskins and Valdes 1990) have pointed out that moist processes are an important aspect of its dynamics. Chang (2006) modifies a primitive equation model in the vein of MM93 to take into account the smaller static stability due to latent heat

Corresponding author address: Alexandre Laîné, Laboratoire de Météorologie Dynamique, ENS, 24 rue Lhomond, 75005 Paris, France.
E-mail: laine@lmd.ens.fr

DOI: 10.1175/2011JAS3618.1

release by moist processes. Whereas numerous studies have shown that moist processes strongly enhance synoptic perturbations when looking at a particular life cycle, there are only a few studies addressing this aspect at a storm-track scale (Zhang 1995; Orlanski 2003; Solomon 2006; Frierson et al. 2006, 2007; Schneider and O'Gorman 2008). The main results were that water vapor affects the stratification of the midlatitude atmosphere by decreasing the eddy activity, but eddies are more able to transport energy to high latitudes through moisture fluxes. The importance of water vapor for the general circulation of the atmosphere can be expected to become even higher since the humidity content of the air is expected to increase under warmer conditions according to the Clausius–Clapeyron relationship. This should greatly impact the whole climate system, as consistently observed within Intergovernmental Panel on Climate Change (IPCC) Fourth Assessment Report (AR4) models (Soden and Held 2006; Held and Soden 2006), and could significantly affect storm-track dynamics (Lapeyre and Held 2004, hereafter LH04). The effect of greenhouse gas (GHG) changes on atmospheric dynamics can be directly considered in state-of-the-art ocean–atmosphere coupled models (Solomon et al. 2007). Nevertheless, it is very difficult to consider the separate roles of the changes in the purely dynamical mean state of the atmosphere, its moisture property changes, and their interaction with storm-track dynamics. Laîné et al. (2009) found the direct effect of latent heat release changes on the eddy energy budget in simulations with $4 \times CO_2$ increase to be of second order compared to baroclinic conversion. However, anomalous latent heat processes are able to indirectly modify the baroclinic conversion term through changes in mean baroclinicity (Hoskins and Valdes 1990) or in synoptic perturbation life cycles (Orlanski 2003; LH04).

To study the role of moist processes in storm tracks, we propose to develop and to use a modified version of the MM93 model, using the approach of LH04 to include moist processes in a QG model. A QG model based on the same principles, but including simplified radiative physics and an ocean component, was also developed (ECBILT; Opsteegh et al. 1998) to simulate climates of the past. Frierson et al. (2006, 2007) have developed a simplified moist version of a dry GCM in which moist effects are included except for their radiative influence, thereby isolating their purely dynamical effects. However, the use of a GCM leads to a more difficult interpretation of the results since the modification of the Hadley circulation due to moist processes may also impact the midlatitude jet (Son and Lee 2005). We believe that a QG moist model is a companion model to state-of-the-art coupled GCMs.

In section 2, we present a moist version (hereafter "moist model") of the MM93 model. Its mean-state characteristics and its intrinsic variabilities are compared in section 3 with those of its dry counterpart (hereafter "dry model") and with the 40-yr European Centre for Medium-Range Weather Forecasts (ECMWF) Re-Analysis (ERA-40). Section 4 is dedicated to the main conclusions.

2. Model description

a. Potential vorticity equations

The model is primarily based on the MM93 QG model (see last paragraph of this subsection for a summary of the main differences). It integrates the prognostic equations for QG potential vorticity (PV) at three levels: $p_1 =$ 200 hPa (level 1), $p_2 =$ 500 hPa (level 2), and $p_3 =$ 800 hPa (level 3). Our moist version consists in adding a latent heating term in the temperature equations and then including the appropriate term in the PV equation, similarly to LH04. The PV equations can be expressed as

$$\begin{aligned}
\frac{\partial q_1}{\partial t} &= -J(\psi_1, q_1) - D_1(\psi_1, \psi_2) + \mathcal{L}_1 + S_1,\\
\frac{\partial q_2}{\partial t} &= -J(\psi_2, q_2) - D_2(\psi_1, \psi_2, \psi_3) + \mathcal{L}_2 + S_2,\\
\frac{\partial q_3}{\partial t} &= -J(\psi_3, q_3) - D_3(\psi_2, \psi_3) + \mathcal{L}_3 + S_3, \qquad (1)
\end{aligned}$$

where q and ψ denote respectively the PV and the streamfunction; J is the Jacobian determinant; and D_i, $\mathcal{L}_i$, and S_i are respectively the dissipation, latent, and forcing terms described hereafter. PV is defined as

$$\begin{aligned}
q_1 &= \nabla^2\psi_1 - \frac{1}{R_1^2}(\psi_1 - \psi_2) + f,\\
q_2 &= \nabla^2\psi_2 + \frac{1}{R_1^2}(\psi_1 - \psi_2) - \frac{1}{R_2^2}(\psi_2 - \psi_3) + f,\\
q_3 &= \nabla^2\psi_3 + \frac{1}{R_2^2}(\psi_2 - \psi_3) + f\left(1 + \frac{h}{H_0}\right), \qquad (2)
\end{aligned}$$

where $R_1 = 650$ km and $R_2 = 400$ km are the Rossby radii of deformation for the 200–500-hPa and 500–800-hPa layers, respectively; $f = 2\Omega \sin\phi$, with ϕ being the latitude; and H_0 is a scale height set to 9 km. Also, h is the topographic height, calculated as the height envelope (mean plus the standard deviation of the topography within each given grid cell from an original resolution of ½°), as described by Lott (1999); D_1, D_2, and D_3 are linear operators representing respectively the effects of Newtonian relaxation of temperature, linear drag on 800-hPa wind, and horizontal diffusion of vorticity and temperature (cf. appendix A of MM93). The different

parameters used in these dissipative terms are the same as in MM93 except for the time scale of the horizontal diffusion, which depends on the spectral resolution (0.1 in T42 compared to 2 days for the T21 of MM93).

The terms $\mathcal{L}_1$, $\mathcal{L}_2$, and $\mathcal{L}_3$ represent the PV changes associated with the release of latent heat from large-scale precipitation. They are expressed as

$$\mathcal{L}_1 = \gamma(\phi)\frac{R_{\text{air}}L_{\text{vap}}}{C_{\text{pd}}f_0}R_1^{-2}\log\left(\frac{p_1}{p_2}\right)\mathcal{P}_{12},$$

$$\mathcal{L}_3 = -\gamma(\phi)\frac{R_{\text{air}}L_{\text{vap}}}{C_{\text{pd}}f_0}R_2^{-2}\log\left(\frac{p_2}{p_3}\right)\mathcal{P}_{23},$$

$$\mathcal{L}_2 = -(\mathcal{L}_1 + \mathcal{L}_3), \tag{3}$$

which is consistent with LH04 (see appendix A for proper derivation). Here R_{air} is the gas constant for dry air, L_{vap} the latent heat of vaporization, C_{pd} the specific heat for dry air, and f_0 the Coriolis parameter at 45°; $\mathcal{P}_{12}$ and $\mathcal{P}_{23}$ represent precipitation rates for the intermediate levels 200–500 and 500–800 hPa, respectively. The next section details the precipitation scheme. In the QG model, latent heating is conceived as a PV forcing, as stated by Eqs. (1) and (3). However, the Coriolis parameter enters in the denominator of $\mathcal{L}_i$ and our parameterization of latent heating is not valid anymore in the tropics. Moreover, the QG assumption is not valid in the tropics (e.g., it does not reproduce the Hadley cell). We therefore use a nondimensional function $\gamma(\phi)$ to avoid PV creation by latent heat release in these regions:

$$\gamma(\phi) = \text{sign}(\phi)\frac{1 + \tanh\{10[\sin(\phi) - 0.5]\}}{2}, \tag{4}$$

where sign(ϕ) indicates the sign of ϕ (positive for the Northern Hemisphere and negative for the Southern Hemisphere). The γ function equals 0 at the equator, stays close to 0 until 20°N (20°S), and then rapidly increases (decreases) to about 1 (-1) near 40°N (40°S) and up to the poles.

As in MM93, S_1, S_2, and S_3 are time independent but spatially varying sources of PV used to equilibrate the model under a given climatology. They are determined by computing the PV tendencies of the QG model using the observations as initial conditions, so the forcing balances the sum of all PV tendencies on average. We have used 4-times-daily geopotential height fields for winter months [December–February (DJF)] from 1967 to 2001 of ERA-40 data. The conversion from geopotential (Φ) to streamfunction fields at each level is obtained from the inversion of the linear Charney balance $\nabla^2\Phi = \nabla \cdot (f\nabla\psi)$.

Our model is similar to MM93 with the addition of PV tendency terms resulting from latent heat release during precipitation and the possibility of higher resolution (T42 is used in this paper with a time step of 1800 s). The differences from the original version concern the topographic height h (which takes into account the height envelope instead of the averaged height, consistent with Lott 1999), smaller Rossby radii of deformation [values are the ones used in Rivière (2009)], and a linear inversion to derive the streamfunction from reanalyzed geopotential heights using Charney balance for the calculation of the forcing terms. None of these changes implies large differences in the results of the model, but they are thought to represent slightly better configurations and were therefore applied.

b. Moisture and temperature equations

The moisture equation that couples the thermodynamics terms of Eq. (3) is

$$\frac{\partial m_{ij}}{\partial t} = -J(\psi_{ij}, m_{ij}) - M_{ij}\omega_{ij} - D_{ij}(m_{ij}) - \mathcal{P}_{ij} + S_{ij}^m, \tag{5}$$

where m_{ij} represents the mean specific humidity of the layer p_i–p_j (with ij = 12, 23). Water vapor is treated at midlevel, similarly to the temperature. It is advected horizontally by the geostrophic wind field at midlevel related to the streamfunction $\psi_{ij} = (\psi_i + \psi_j)/2$. In the QG approximation, it is assumed that the static stability is constant in the temperature equation (which allows us to define the Rossby deformation radius). In the same manner, we choose a vertical moisture gradient constant in space and time M_{ij}. As shown by LH04, this would allow us to define a moist enthalpy variable and, for a saturated atmosphere, the effective Rossby deformation radius would be diminished in the precipitating regions. The vertical velocity ω_{ij} is computed at midlevel using a diagnostic omega equation as in LH04, and as described in appendix B. The values used in the model are $M_{12} = -1.51 \times 10^{-5}$ kg kg^{-1} hPa^{-1} and $M_{23} = -1.21 \times 10^{-5}$ kg kg^{-1} hPa^{-1}, which are larger than climatological values by an order of magnitude ranging from 1 to 10 depending on the location. This compensates underestimates of ω_{ij} since frontogenetic ageostrophic motions are not included in the QG model. The M_{ij} values have been adjusted so that the standard deviation of the synoptic variations of the vertical advection term $M_{ij}\omega_{ij}$ has the same order of magnitude as the standard deviation of $\omega\partial m/\partial p$ calculated from reanalyses.

In Eq. (5), D_{ij} represents dissipation effects and consists of the sum of the same scale-selective horizontal diffusion H_i as in MM93 but applied to m_{ij}, and a relaxation term m_{ij}/τ_m, with τ_m = 10 days. This allows us to consider the forcing as a restoring term against some

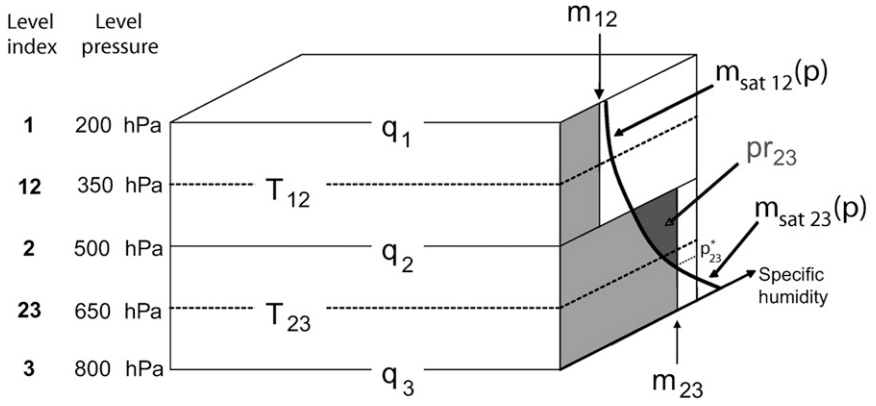

FIG. 1. Simplified sketch of the model. See text for notations and details.

climatology, similarly to the PV equation (MM93). Also, S_{ij}^m is a forcing term calculated in the same way as for the PV equations, and $\mathcal{P}_{ij}$ is the precipitation for the layer p_i–p_j.

The precipitation scheme is based on a simple parameterization of large-scale precipitation such that moisture condenses whenever it reaches saturation (using the Clausius–Clapeyron relationship). We found that if we only consider a saturation threshold depending on the mean temperature of the layer, the precipitation only occurs in very cold regions near the poles. To construct a better scheme, we assume that the specific humidity m_{ij} is constant within the layer (Fig. 1) but that the temperature varies within the layer such that the humidity saturation value varies also. As a result, only a fraction of the layer can precipitate.

The value of moisture at saturation depends on temperature. This latter quantity can be expressed as

$$T = \langle T \rangle - \frac{1}{R_{\text{air}}} \frac{\partial \Phi'}{\partial \log p}, \tag{6}$$

where $\langle T \rangle$ denotes the spatial-mean temperature over the entire sphere and the second term on the rhs corresponds to the hydrostatic balance in height coordinate. The latter term is computed at 350 and 650 hPa using finite differences. The geopotential anomaly (from horizontal mean) Φ' can be retrieved through the Charney balance $\nabla^2 \Phi' = \nabla \cdot (f \nabla \psi)$. The time evolution of the spatial-mean temperature $\langle T_{ij} \rangle$ (corresponding to the 350- and 650-hPa levels) is given by

$$\frac{\partial \langle T_{ij} \rangle}{\partial t} = \frac{L_{\text{vap}}}{C_{\text{pd}}} \langle |\gamma(\phi)| \mathcal{P}_{ij} \rangle + S_{ij}^T - \frac{\langle T_{ij} \rangle}{\tau}. \tag{7}$$

The relaxation time scale τ is the same as in the PV equation (τ = 25 days). Note that τS_{ij}^T serves as the temperature toward which relaxation is done (same for the PV and moisture relaxation terms). The temperature forcing term S_{ij}^T is computed in the same way as the other forcing terms S_{ij}^m and S_i in Eqs. (1) and (8). The initial mean temperature is the winter climatological mean.

The saturation value for water vapor is equal to

$$m_{\text{sat}}(x, y, p) = \frac{R_{\text{air}} p_{s0}}{R_v p} \exp\left[-\frac{L_{\text{vap}}}{R_v T(x, y, p)} + \frac{L_{\text{vap}}}{R_v T_0} \right], \tag{8}$$

where R_v = 461 J K^{-1} kg^{-1} is the gas constant for water vapor and p_{s0} = 6.11 hPa is the reference saturation vapor pressure at T_0 = 273.15 K. Since temperature is calculated only at midlevels and saturation profiles are needed within each layer (200–500 or 500–800 hPa), we extrapolate temperature at the levels 200, 500, and 800 hPa using a constant vertical temperature gradient $\partial T/\partial \log p = [T(x, y, p_{12}) - T(x, y, p_{23})]/\log(p_{12}/p_{23})$ from the knowledge of T_{ij}. We therefore get m_{sat} at three levels within each layer (200, 350, and 500 hPa or 500, 650, and 800 hPa), allowing an approximation of the vertical distribution of saturated moisture as a second-order polynomial in pressure within each layer: $m_{\text{sat}}(x, y, p) = A(x, y) + B(x, y)p + C(x, y)p^2$. We then find the level p_{ij}^* where $m_{\text{sat}}(x, y, p_{ij}^*) = m_{ij}(x, y)$ and integrate the excess of moisture from this level upward to obtain the precipitation rate for the given time step Δt of the model; that is,

$$\mathcal{P}_{ij} = \frac{1}{\Delta t \, \Delta p} \int_{p_{ij}^*}^{p_i} (m_{ij} - A - Bp - Cp^2) \, dp, \tag{9}$$

where Δp = 300 hPa. This corresponds to the darker section in Fig. 1. (In some rare occasions, saturated moisture does not decrease with pressure).

3. Model results

All the simulations have been run at T42 resolution for 3500 days, from which only the last 3000 days are used in the analyses.

a. Climatology

1) ZONAL WIND

Figures 2a–c show the mean zonal wind at 200 hPa (filled gray contours) for, respectively, ERA-40 data and the moist and dry models. The jet intensity in ERA-40 peaks in the western North Pacific over Japan at more than 70 m s^{-1}, whereas the models simulate a weaker zonal wind maximum (around 60 and 65 m s^{-1} for the moist and dry models, respectively) and a latitudinal spread in this area too much to the north compared to ERA-40 (see Figs. 3a,b). The westerlies in the eastern Pacific cover a large band of latitudes in the reanalyses whereas they are more concentrated in the northern part around 60°N in the models. In the Atlantic, the jet maximum is realistically located in the models over the eastern coast of North America, but it is too weak in the moist model. The flow exhibits a double-jet structure in the eastern part of the oceanic basins that is well represented in the models, especially in the moist model.

The 200-hPa zonal wind of the moist model essentially differs from its dry model counterpart by a general deceleration (Figs. 2b,c), which can reach more than 10 m s^{-1} (Fig. 3c). A slight increase in upper-level subtropical westerlies is found in the moist model (compared to its dry counterpart), especially in the eastern part of the oceanic basins and over the western North Pacific, with values reaching about 5 m s^{-1} (Fig. 3c). The differences in zonal wind with ERA-40 are larger in the dry model (Fig. 3b) than in the moist model (Fig. 3a). This is due to the general northern attenuation and southern enhancement of the zonal wind in the moist model compared to the dry one. However, the moist model has a too small intensity in zonal wind in the jet-core regions.

2) WAVE BREAKING

Part of the characteristics of the midlatitude jets depends on the nonlinear eddy feedbacks through eddy momentum and temperature horizontal fluxes. The sign of the eddy momentum fluxes is closely related to the shape of the baroclinic waves and the way they break. We usually distinguish between anticyclonic (AWB or LC1) and cyclonic (CWB or LC2) wave breaking (Thorncroft et al. 1993). An AWB is characterized by positive momentum fluxes and tends to accelerate the jet poleward, whereas the reverse is true for a CWB.

Wave-breaking (WB) diagnostics have been recently shown to be a useful tool to interpret the climatological locations of the eddy-driven jets (Wernli and Sprenger 2007; Strong and Magnusdottir 2008; Rivière et al. 2010), as well as their fluctuations due to ENSO, the North Atlantic Oscillation (NAO), or the Pacific–North America pattern (PNA) (Benedict et al. 2004; Orlanski 2005; Rivière and Orlanski 2007; Martius et al. 2007). Here CWB and AWB events are detected from instantaneous maps of absolute vorticity using the algorithm presented in Rivière (2009).

The occurrence of AWB (thick black contours in Figs. 2a–c) is accurately located in the models (southeastern part of the storm tracks), although eddies tend to break too quickly in the Atlantic region, associated with positive anomalies in AWB occurrence off the eastern coast of North America and a deficit in AWB farther southeastward (Figs. 3a,b). The magnitude in the frequency of occurrence of AWB is relatively correct in the Atlantic whereas it is too large in the Pacific region. In terms of cyclonic wave breaking (thick white contours in Figs. 2a–c), both QG models tend to underestimate their occurrence. A bias toward excessive AWB compared to CWB is expected in the dry QG model partly because of the use of the constant Coriolis parameter in the stretching part of the PV (Rivière 2009). In the moist model, however, latent heating, which is mainly released along the fronts of the cyclonic eddies, should strengthen the cyclones while having little direct effect on anticyclones, as shown by LH04 in QG simulations of baroclinic turbulence. This asymmetry should favor the occurrence of CWB (Orlanski 2003). As expected, a larger occurrence of CWB takes place in the moist model than in its dry counterpart and is consistent with results of Orlanski (2003) using a high-resolution primitive equation model. This partly compensates for the deficit in CWB compared to reanalyses in the dry model, although not entirely. Also, the moist model does not reduce the bias toward too much AWB. We therefore conclude that the purely dynamical biases associated with the QG approximation remain although CWB is better reproduced in the moist QG simulation.

Figures 3a and 3b show that it is possible to relate the biases in zonal wind properties between the models and the reanalyses to WB biases. First, zones of more (less) frequent WB occurrence are associated with negative (positive) zonal wind anomalies for both types of wave breaking. The physical link can be directly inferred from the definition of a WB event in the detection algorithm, which consists of a reversal of the meridional absolute vorticity gradient and hence of the zonal wind direction. With regard to eddy momentum fluxes associated with WB events and their impact on the zonal wind, the more frequent occurrence of AWB in the southern part of the jet and the less frequent occurrence of CWB to the north of it in the models (e.g., especially in the Pacific region) are related to a northward jet

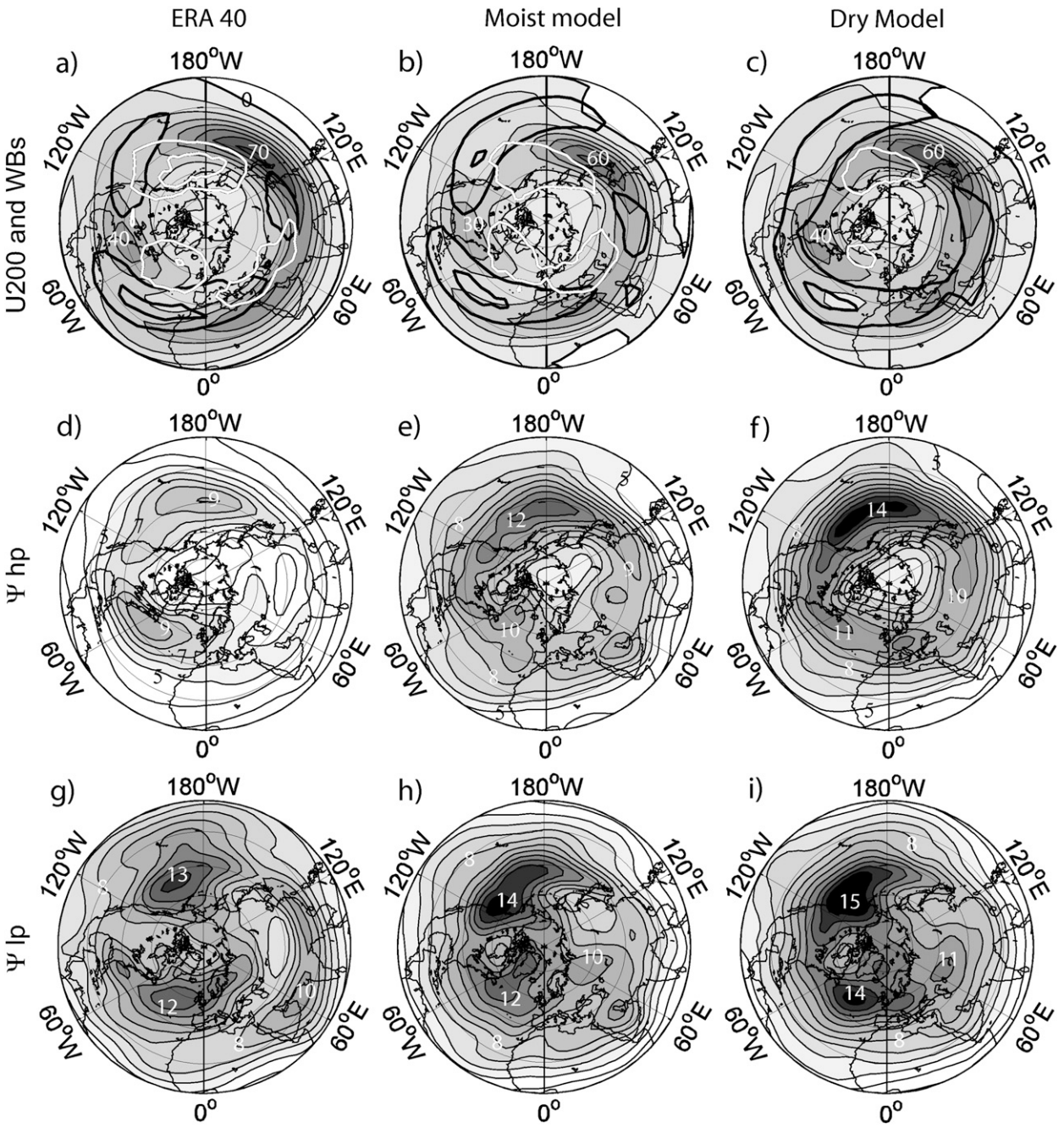

FIG. 2. (a)–(c) Zonal wind (m s^{-1}) and wave breaking frequencies of occurrence for AWB (black contours every 0.1 day^{-1}) and CWB (white contours every 0.05 day^{-1}) at 200 hPa for (a) ERA-40 (DJF 1967–2001), (b) the moist model, and (c) the dry model. (d)–(i) Standard deviation of the variability of the streamfunction (m^2 s^{-1}), vertically averaged (using 800-, 500-, and 200-hPa levels), for (d),(g) ERA-40 and (e),(h) the moist and (f),(i) the dry versions of the model, for (d)–(f) synoptic-scale variability and (g)–(i) low-frequency variability.

intensification, as expected. Note that there might be a positive feedback between the type of wave breaking and the jet latitude as pointed out in Rivière (2009), with a more northward jet tending to favor AWB rather than CWB. In the North Atlantic, the relationship between the biases in the type of WB and in zonal wind is also consistent.

The direct relationship between too many (too few) WB occurrences and negative (positive) zonal wind anomalies still generally holds in the comparison

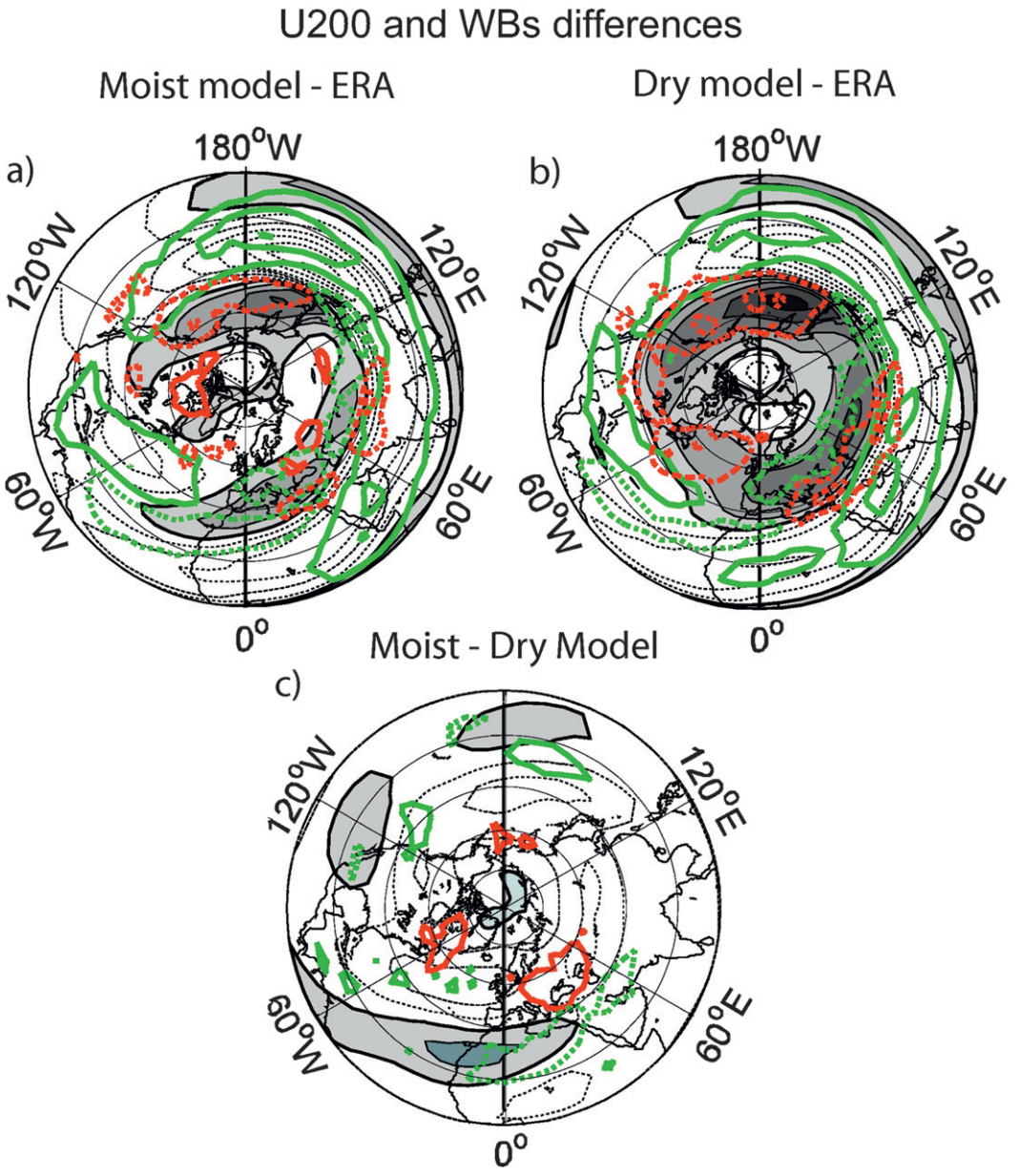

FIG. 3. Differences of 200-hPa zonal wind (m s^{-1}) and wave breaking frequencies of occurrence between (a) the moist model and ERA-40, (b) the dry model and ERA-40, and (c) the moist and the dry model. Contours with gray shading are wind anomalies, with contours every 5 m s^{-1}; the zero contour is the thickest and corresponds to the limit between white and gray shadings (white for negative, gray for positive). Green contours indicate anomalies for AWB (contours every 0.05 day^{-1} beginning at 0.025 day^{-1}); red contours are anomalies for CWB (contours every 0.025 day^{-1}). Dashed contours indicate negative values.

between the dry and moist models (Fig. 3c). Note that more AWB events in the moist model in the Pacific sector are accompanied by not only a local deceleration but also an acceleration of the westerlies to the south in the subtropics. Indeed, when a given WB event occurs, acceleration zones are usually present on both sides of the WB zone [see, e.g., Fig. 20 of Rivière (2009)]. One is stronger and related to the acceleration of the eddy-driven jets, but a weak secondary acceleration is often present on the other side of the breaking area. Nevertheless, WB characteristics do not explain all zonal wind anomalies in Fig. 3c. In particular, the central part of the negative jet anomalies in the Pacific region around 40°N, 180°W cannot be related to a significant change in WB

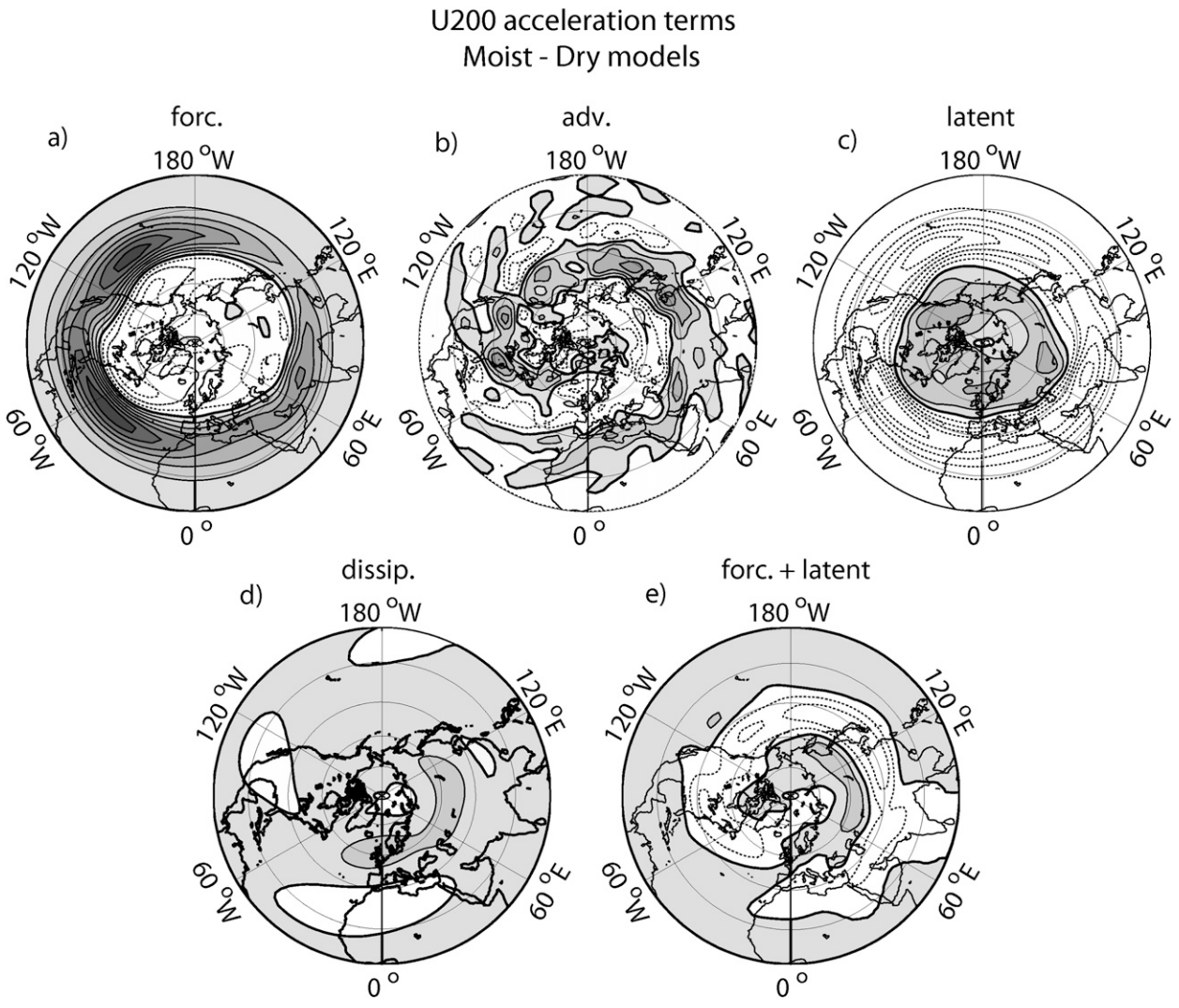

FIG. 4. Differences of the terms from the 200-hPa zonal wind Eq. (10) between the moist and the dry models. Contours are every 5×10^{-6} m s^{-2}; the zero contour is thicker; negative values are indicated as white and contain dashed contours. See text for more details.

events since the positive anomalies of AWB south of it and of CWB north of it would have resulted in zonal wind acceleration in the jet-core region.

3) ZONAL WIND TENDENCIES

Since WB diagnostics are not able to explain the zonal wind deceleration in the jet-core regions from the dry to the moist model, a more systematic analysis is made from Eq. (1). The different terms of this equation can be directly associated with wind acceleration considering the transformation from QG potential vorticity to wind tendencies. To this end, from the definition of PV [Eq. (2)], we can relate the streamfunction ψ_i to the PV anomaly q'_i (from a resting atmosphere), writing $q'_i = \mathcal{M}_{ij}\psi_j$ and $\psi_i = \mathcal{N}_{ij}q'_j$, where $\mathcal{N}$ is the inverse of $\mathcal{M}$ (easily defined in spectral space) and where sums over j components are implicit. The zonal velocity tendency equation is obtained from Eq. (1) as

$$\frac{\partial u_i}{\partial t} = \frac{\partial[\mathcal{N}_{ij}J(\psi_j, q_j)]}{\partial y} + \frac{\partial(\mathcal{N}_{ij}D_j)}{\partial y} - \frac{\partial(\mathcal{N}_{ij}\mathcal{L}_j)}{\partial y} - \frac{\partial(\mathcal{N}_{ij}S_j)}{\partial y}, \tag{10}$$

since $u_i = -\partial\psi_i/\partial y$. Figure 4 shows the differences between the moist and the dry models of the terms on the rhs of Eq. (10) at 200 hPa. In statistical equilibrium, the temporal mean of the lhs term is zero such that all terms on the rhs cancel each other. The dissipation term can be thought as a relaxation of the zonal wind so that its pattern (Fig. 4d) is broadly opposite to the pattern of the

200-hPa zonal wind (Fig. 3c) when comparing moist minus dry differences. This allows us to interpret the other terms in Eq. (10) as acting as accelerating or decelerating the jet comparing moist and dry simulations. The term associated with the PV advection (and therefore with Eliassen–Palm fluxes; Andrews and McIntyre 1976) alone (Fig. 4b) cannot explain the deceleration of the jet maxima in the moist model compared to the dry model. On the contrary, it reflects an acceleration in the jet-core regions and deceleration on the flanks of the jets in the moist model as already seen with the WB diagnostics. The difference in forcings between the moist and the dry models (Fig. 4a) does not explain it either since it leads to a general acceleration on the southern flank of the jet and a deceleration on the northern flank. The deceleration in the central part of the jet in the moist model is due to the latent heat release term (Fig. 4c).

In the dry model, the forcing implicitly takes into account a stationary latent heating, whereas in the moist model this latent heating is explicit and is tightly related to synoptic variability. It is thus more interesting to compare the sum of the forcing and latent heating terms. Figure 4e shows that the variable latent heat effect has a larger contribution than the forcing term alone. The presence of the persistent precipitation in the storm track of the moist model increases latent heat release to the north of the jet, thereby warming the atmosphere there and leading to a deceleration of the jet through thermal wind balance.

4) MOISTURE VARIABLES

The mean specific humidity fields in ERA-40 and in the moist model are presented in Figs. 5a and b. The main characteristics are realistically reproduced in the model, with a poleward reduction in specific humidity, strong latitudinal gradients over the wind jet maxima regions, and a broadening of the gradient east of them. Nevertheless, biases are found in the model, especially with too weak latitudinal gradients in the western part of the oceanic basins and stronger values in the southeastern part of them (Fig. 6a for differences). Some of these differences correspond to temperature biases in the mid- and high latitudes, consistent with a temperature control on humidity through saturation values (Figs. 6a,b). In the eastern part of the continents and in high latitudes, too warm temperatures compared to ERA-40 result in too much water vapor due to too high saturation values.

In terms of large-scale precipitation (Figs. 5c,d), the order of magnitude and the large-scale features of the observed midlatitude climate are roughly reproduced in the model, especially with strong precipitation in storm-track regions. Nevertheless, biases exist: too strong values appear in general (by about a factor of 2), and more particularly over localized areas in Europe and Asia, and precipitation rates associated with the Pacific storm track are too much to the east. The lack of precipitation in the central Pacific in the model is consistent with the positive temperature anomalies in this area (Fig. 6b) that raise the moisture saturation value. The lack of precipitation in the central Pacific may also explain the excess precipitation farther eastward through anomalous moisture advection. An eastward shift of the Pacific precipitation zone is also present in the ECBILT model, which also consists of a simple moist version of the MM93 model [see Fig. 5a of Opsteegh et al. (1998)]. However, contrary to our results, ECBILT tends to have weaker precipitation rates than reanalyses in general, with precipitation less localized in storm-track regions.

5) HIGH-FREQUENCY AND LOW-FREQUENCY EDDY ACTIVITY

The high-frequency variability represents the synoptic-scale variability associated with atmospheric perturbations. Figures 2d–f show the standard deviation of the high-frequency variability of the streamfunction, averaged over the three levels. To obtain these maps, we filter daily output by subtracting a 7-day running average to the time series. The models overestimate the eddy activity by about 50% in the moist model and about 70% in the dry model in the Pacific region; nevertheless, the patterns are realistic, especially for the moist model, with a peak of activity around the date line. The North Atlantic storm track is not successfully reproduced by both QG models with a lack of separate activity from the Pacific storm track. This could be partly due to a lack of low-level baroclinicity associated with SST frontal zone, which is known to energize the North Atlantic storm tracks (e.g., Nakamura et al. 2004). Differences in the high-level mean-flow baroclinicity (not shown) cannot account for the differences between the models and the reanalyses (weaker baroclinicity but stronger eddy activity in models compared to reanalyses) but seem consistent with the differences between the models. The decrease in eddy activity despite the presence of moisture, which allows extra eddy potential energy input during storm formation through latent heat release, is similar to the GCM results of Frierson et al. (2006, 2007). As in their case, the decrease in baroclinicity is responsible for the decrease in eddy activity under moister conditions.

The characteristics of the synoptic variability of specific humidity are shown in Figs. 5e and 5f for ERA-40 and the moist model. The pattern of synoptic moisture variability is relatively well reproduced in the model compared to reanalyses, especially in the Pacific region, with a peak occurring around 170°E. In the North Atlantic, the model suffers from the lack of synoptic

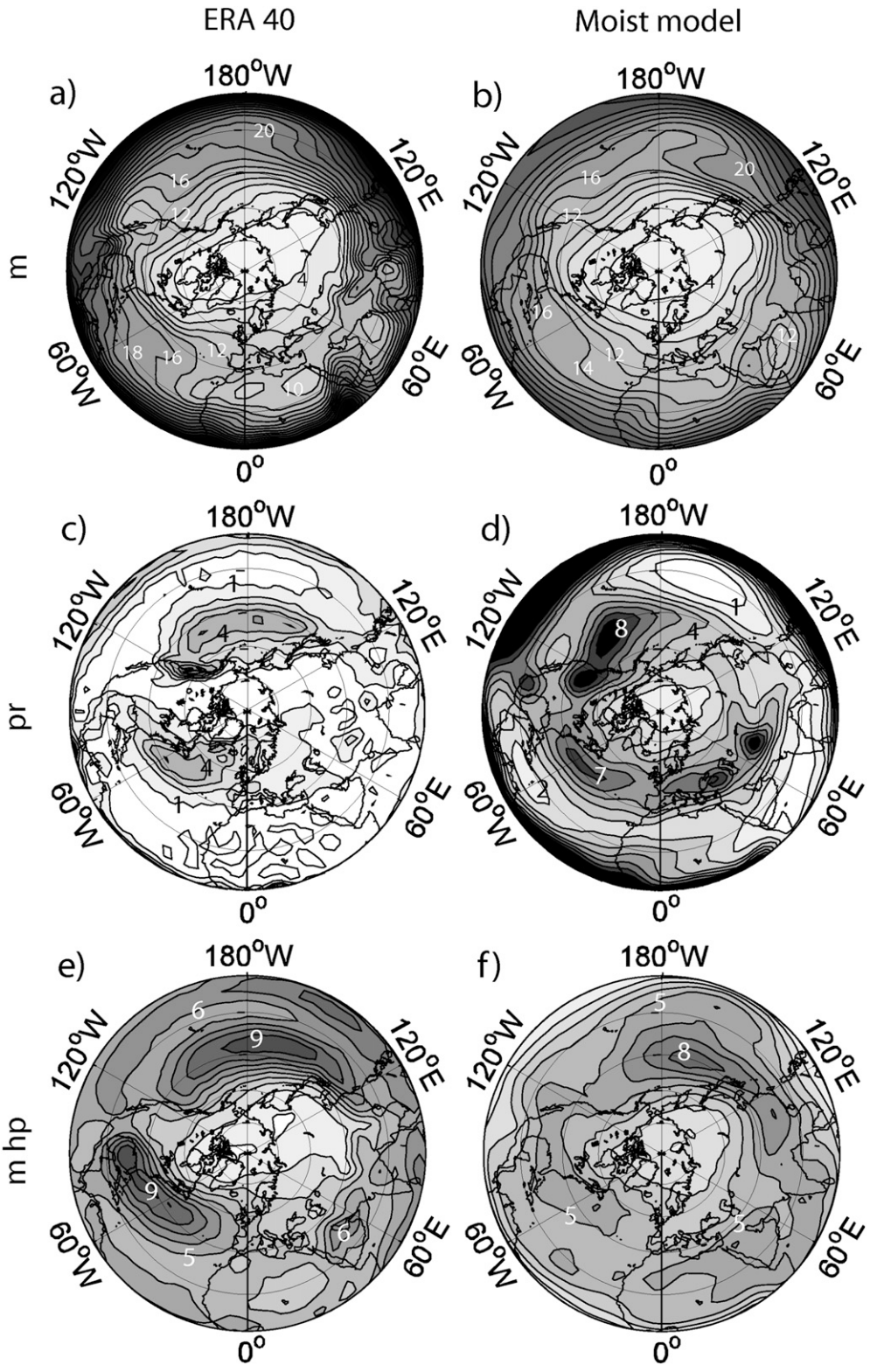

FIG. 5. (a),(b) Mean specific humidity (10^{-4} kg kg^{-1}), vertically averaged (using the 800–500- and 500–200-hPa layers) for (a) ERA-40 and (b) the moist model. (c),(d) Mean precipitation rate (mm day^{-1}) and (e),(f) vertical average of the standard deviation of the synoptic variability of the specific humidity (2.5×10^{-4} kg kg^{-1}) for ERA-40 (DJF; large-scale precipitation) and the moist model, respectively.

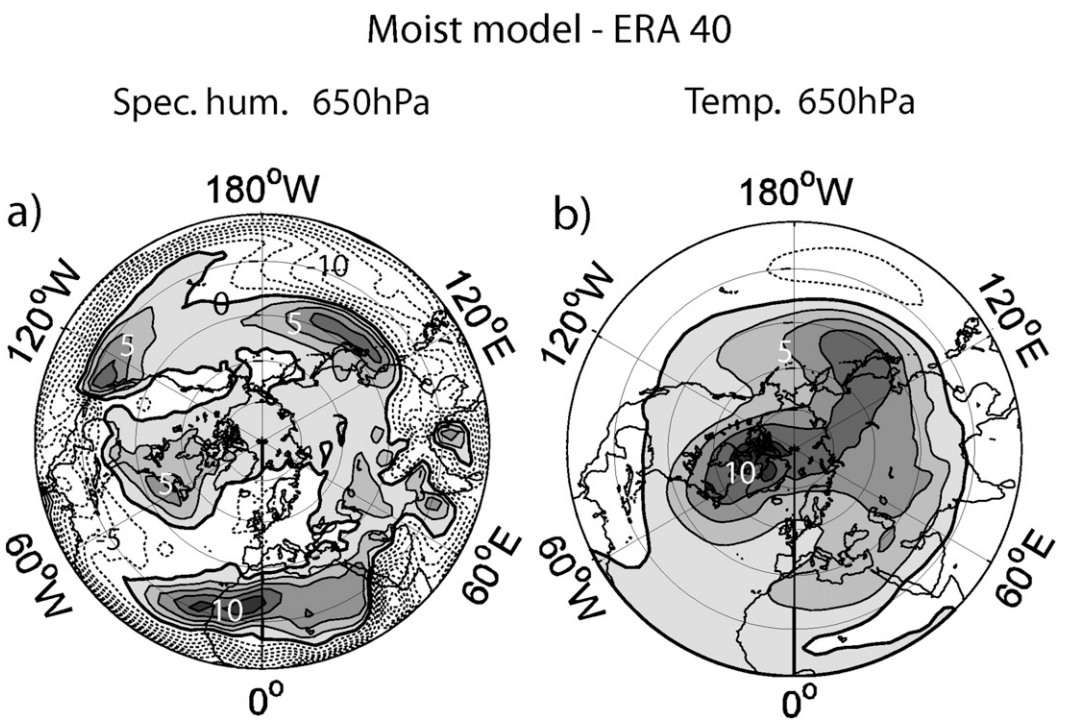

FIG. 6. Differences between the moist model and ERA-40 for (a) 650-hPa mean specific humidity (contours every 2.5×10^{-4} kg kg^{-1}) and (b) 650-hPa mean temperature (contours every 2.5 K). The zero contour is thick; negative values are white and contain dashed contours.

variability of the North Atlantic storm track, but the pattern of moisture variability is relatively realistic. The different processes influencing the synoptic variability of specific humidity are related to the eddy moisture advection by the mean flow and by the eddies themselves and to evaporation and precipitation associated with the perturbations. Our model uses S_{ij}^m to supply humidity [Eq. (5)] that can be thought of as representing evaporation effects and mean vertical fluxes that are not represented by the QG vertical motions (such as in the Hadley cell). This fixed term does not provide high-frequency variability contrary to the reanalyses. This can explain a general deficiency in the specific humidity variability in the model despite stronger dynamical variability (Figs. 2d,e). The generally well-located moisture variability highlights that the eastward shift in precipitation associated with the Pacific storm track is not due to a bias in dynamical variability but rather to biased saturation levels. Indeed, temperature biases between the moist model and ERA-40 north of 30°N (Fig. 6b) are weaker in the eastern Pacific than in the central Pacific, which leads to more precipitation in the former region than in the latter.

The mean low-frequency variability, diagnosed using the standard deviation of the 7-day running mean of the vertically averaged streamfunction time series (Figs. 2g–i), is located in the eastern part of the two main Northern Hemisphere storm tracks. It is the case for both ERA-40 and the models. The low-frequency variability is slightly higher by about 10%–20% in the models than in ERA-40, especially for the dry model. In terms of patterns, the dry model simulates very realistic structures and the moist model slightly shifted ones: too far eastward in the Pacific region and too far northward in the North Atlantic.

b. Weather regimes

1) CLUSTER ANALYSIS

To gain a deeper insight into the low-frequency characteristics, we perform a cluster analysis using the *k*-means method. Objective tests on ERA dataset are performed to assess the relevance of Northern Hemispheric regimes and to determine the numbers of principal components (PCs) and of clusters to be chosen.

To partition data into *k* clusters, *k* random fields (called the initial seeds) are chosen among the data. The algorithm (Michelangeli et al. 1995) looks for a minimization of the sum of the variances in each cluster. Because the result of the partition depends on the initial random seeds, this step is repeated 100 times and the best partition is chosen among them. Then we construct random

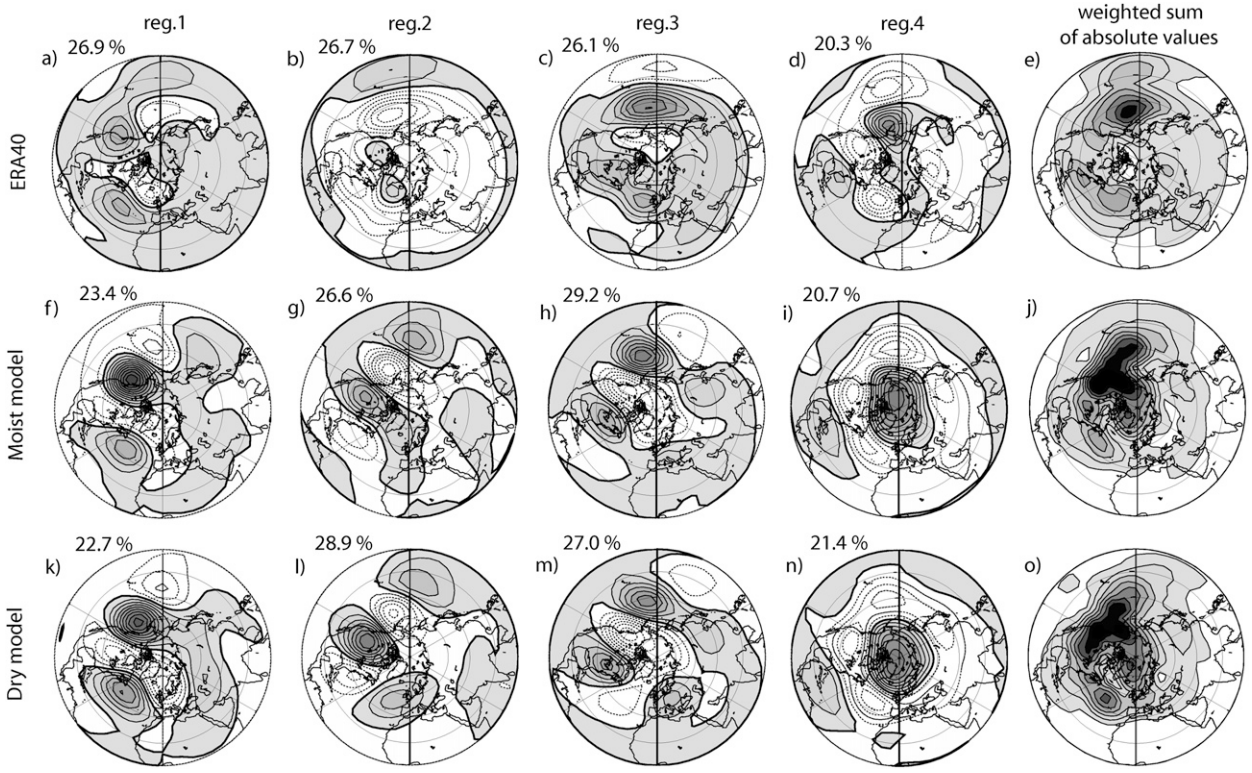

FIG. 7. Composite of the four weather regime patterns obtained from the first six PCs of the daily streamfunction at 500 hPa for (a)–(d) ERA-40, (f)–(i) the moist model, and (k)–(n) the dry model. Contours are every 2.5 $m^2\ s^{-1}$; the zero contour is thick; negative values are white and contain dashed contours. (e),(j),(o) Weighted mean (depending on the percentage of points assigned with a cluster) of the absolute value of the four regime patterns. Contours are every 5 $m^2\ s^{-1}$ beginning at 5 $m^2\ s^{-1}$.

time series so that they have the same variance, first-order autocorrelation (red noise), and cross correlations as the input ERA-40 PCs. We compare the mean spatial correlation of the cluster patterns obtained from the ERA-40 dataset and for the 95th percentile obtained from random time series. We consider the test is passed when the correlation is greater for the actual time series than for the 95th percentile of noise time series. This test is similar to that of Michelangeli et al. (1995). We performed the test for 2–10 regimes and for 3, 6, and 9 PC inputs from daily 500-hPa streamfunction from 20° to 90°N for ERA-40 reanalyses interpolated over a T42 grid and taking only one grid point over two in both latitude and longitude in order to isolate large-scale structures. The cluster analysis passes the test for 6 and 9 PCs and 4 regimes. We hereafter use 6 PCs and 4 regimes to perform the cluster analysis and determine the regimes. Note that the models did not pass the test, but the same parameters are used for comparison.

Figures 7a–d show the four regimes (hereafter denoted as regimes 1, 2, 3, and 4, respectively) obtained from ERA-40 along with the percentage of points composing the different clusters. Despite relative amplitude differences between the maxima within some regime patterns, the four clusters (regimes 1, 2, 3, and 4) correspond respectively to clusters A, D, B, and C of Corti et al. (1999) and to regimes ZNAO, PNA, BNAO, and RNA of Kimoto and Ghil (1993). Although different datasets are used in these studies, the identification of similar patterns indicates the robustness of the results. The daily atmospheric configurations are almost equally distributed among the four regimes, except for a slightly lower distribution within the fourth cluster (Fig. 7d; about 20%). Figure 7e shows the sum of the absolute value of the streamfunction anomalies associated with each regime and weighted by its relative occurrence. It indicates the part of the variability explained by the four regimes only. The good match between Fig. 7e and the low-frequency variability of Fig. 2g indicates the relevance of interpreting the low-frequency variability in terms of these four regimes.

The first cluster exhibits four main streamfunction anomaly centers (Fig. 7a): two distributed meridionally in the Atlantic, corresponding to a positive NAO phase, and two distributed zonally in the eastern Pacific, corresponding to an intensified Aleutian low and anomalous northward winds off the western North American

coast, corresponding in turn to a positive PNA phase. The assignment of models regimes to their corresponding ERA-40 counterparts has been performed subjectively by considering the shape, localization, and successions of the main anomaly centers in midlatitudes. The two models reproduce reasonably well the first regime patterns (Figs. 7f,k), but with strong biases (usually positive) in the anomaly amplitudes, especially for the positive anomaly center over the western North American coast. The axis of the anomaly centers also tends to be shifted in the southwest–northeast direction in the models compared to ERA-40. The differences between the models are much weaker than the differences with respect to ERA-40. ERA-40 regime 2 (Fig. 7b) exhibits zonal anomalies that correspond to a strongly intensified Aleutian low and a reduced Icelandic low in the Atlantic. It corresponds to the negative phase of the Arctic Oscillation (AO), although the anomaly centers are not precisely collocated with the AO ones, especially for the negative anomalies in the Atlantic region, which are located more westward along the eastern North American coast in the regime. The corresponding regimes simulated by the models (Figs. 7g,l) contain strong biases, and the zonal structure disappears because of the intrusion of strong positive anomaly centers between the main negative ones, showing characteristics of a wave train. ERA-40 regime 3 (Fig. 7c) corresponds to some extent to the opposite structure of regime 2 in the Pacific but not in the North Atlantic. In the Pacific, the pattern is similar to the positive phase of the AO with a strongly reduced Aleutian low, whereas in the Atlantic the negative anomaly around the Icelandic low is weak, the strongest anomaly being a positive center off Ireland. Similarly to regime 2, the simulations of regime 3 exhibit a stronger negative anomaly center between the positive ones compared to reanalyses. Finally, ERA-40 regime 4 (Fig. 7d) is relatively similar to the opposite phase of regime 1 in the Pacific and to regime 2 in the Atlantic. Over the Pacific Ocean, the Aleutian low is reduced, and negative anomalies are found eastward over western North America, corresponding to anomalous southward winds along its western coast. Negative anomalies are also found south of the positive anomalous center, further decreasing the jet in the central Pacific. In the models, the structure is more zonal, shifted northward in the central North Pacific but reproduced accurately in the Atlantic sector.

2) WIND PATTERNS AND WB PROPERTIES ASSOCIATED WITH THE REGIMES

Figure 8 shows the zonal wind patterns and the AWB and CWB frequency of occurrence associated with each regime. The differences in WB properties and wind anomalies are consistent with the meridional displacement of the eddy-driven jet associated with the type of breaking. In the northeastern Pacific, for ERA-40, the northward position of a jet separated from the subtropical jet (double jet structure) in regimes 1 and 3 (Figs. 8a,c) is related to a greater occurrence of AWB and a lower occurrence of CWB compared to regimes 2 and 4. In the latter cases, the southern position of a single jet is associated with lower (greater) occurrences of AWB (CWB). In the models, the double-jet structure of regimes 1 and 3 in the northeastern Pacific is well reproduced (except for regime 3 in the dry model) and related to more AWB than in regimes 2 and 4. Regime 2, which was poorly reproduced in terms of streamfunction anomalies in the models, is also poorly reproduced in terms of jet and WB characteristics. For ERA-40 and the models, regime 4 is characterized by greater (lower) CWB (AWB) occurrences than the other regimes, consistent with a relatively southward position of a single jet.

In the North Atlantic, for ERA-40, the clearest double jet structure appears in regime 1. It is associated with greater (lower) AWB (CWB) occurrences than for the other regimes. The two models accurately reproduce the double jet structure and the associated WB characteristics of regime 1 (Figs. 8e,i), typical of the positive phase of the NAO. Similar properties in jet position and WB frequencies are found between ERA-40 and the models for the other regimes, except for regime 2, which is poorly represented in the dry model in particular.

WB characteristics are consistent with the different wind patterns associated with the regimes. This highlights the role of the eddy forcing on the mean flow associated with the low-frequency variability in ERA-40 and the models. All the regimes present local latitudinal shifting and/or pulsing of the Pacific and Atlantic eddy-driven jets. We have checked similarly to Rivière et al. (2010) that there exists a close relationship between a local southward (northward) displacement of the jet and more CWB (AWB) occurrences in the same region. Major biases between the models and ERA-40 can be related to different WB characteristics, although other mechanisms must also account for the strong anomalies in the magnitude of the streamfunction patterns in Fig. 7. The simplified models used here, of course, lack many components that can influence the low-frequency variability, such as oceanic feedbacks (e.g., ''reemergence'' of SST anomalies from one winter to another; Alexander et al. 1999), the tropical variability [e.g., ENSO or the quasi-biennial oscillation (QBO)], or the stratosphere.

3) PRECIPITATION ANOMALIES ASSOCIATED WITH THE REGIMES

Figure 9 shows the precipitation anomalies associated with each regime in ERA-40 (Figs. 9a–d) and the moist

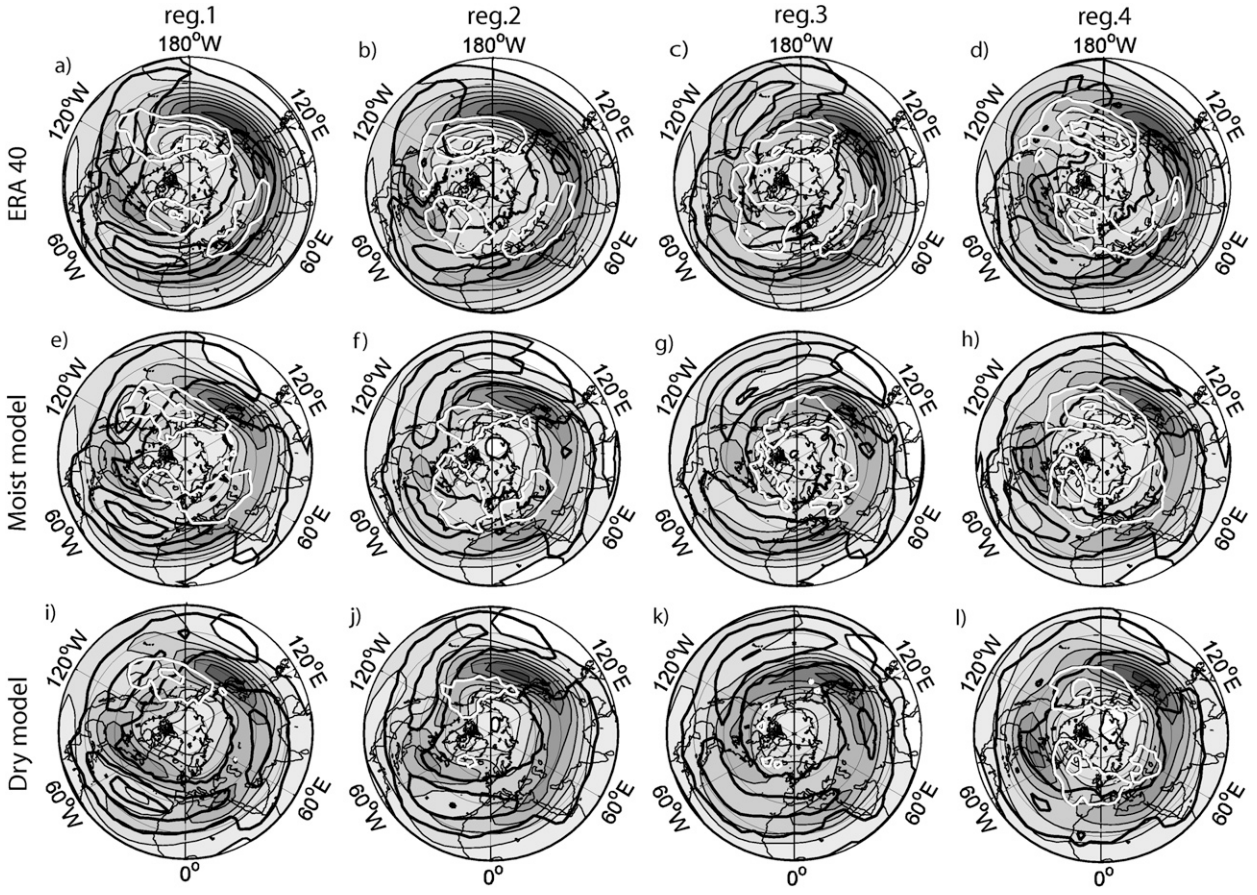

FIG. 8. Composite of the 200-hPa zonal wind speed (gray shading with contours every 10 m s^{-1}), AWB (thick black contours every 0.1 day^{-1}), and CWB (white contours every 0.05 day^{-1}), associated with the regimes presented in Fig. 4, for (a)–(d) ERA-40, (e)–(h) the moist model, and (i)–(l) the dry model.

model (Figs. 9e–h). In ERA-40, the main precipitation anomalies can be related to anomalous meridional flow advection: the northward anomalous advection of moist warm air to colder location favors condensation and precipitation (e.g., in the northeastern Pacific for regimes 1 and 2, or in the eastern Atlantic for regime 4; Figs. 7 and 9a,b,d) and the southward anomalous advection of dry cold air to warmer latitudes reduces precipitation (e.g., in the central Pacific for regime 2 or in the eastern Pacific in regimes 3 and 4; Figs. 7 and 9b–d). The same mechanism also takes place in the model; this is particularly clear in the North Pacific where north–south flow anomalies are the strongest (Figs. 7f–h and 9e–g).

Another apparent feature of the precipitation anomalies concerns their increase or decrease associated with stronger or weaker zonal wind patterns. This can occur for latitudinal shifts and/or intensification/reduction of the jet. A first example can be observed in the Pacific region for regime 3 in ERA-40 where the flow anomalies correspond to a general latitudinal displacement of the jet (cf. streamfunction anomalies of Figs. 7c centered around the mean jet flow near 40°N in the central Pacific), with a similar latitudinal shift in precipitation (anomalies of opposite signs in the northern and southern part of the mean precipitation pattern in Fig. 9c). This is consistent with more (less) precipitation where (from where) the jet has been displaced. Another example, consisting of an intensified or reduced jet, can be seen in the Atlantic for regime 1 (Fig. 8a) and is associated with more precipitation where the jet is increased and also downstream of it because of stronger eastward advection and extended storm track (Fig. 9a). The link between the zonal wind and the precipitation anomalies is also simulated by the model, which can be seen, for example, in regime 4 for a southward displacement of the jet and precipitation zones in the North Pacific (Figs. 7i and 9h), or a jet reduction and associated precipitation along the eastern coast of North America for regime 3 (Figs. 8g and 9g).

The model simulates correctly mechanisms associated with anomalous precipitation, despite mean biases in amplitude or localization of the storm tracks.

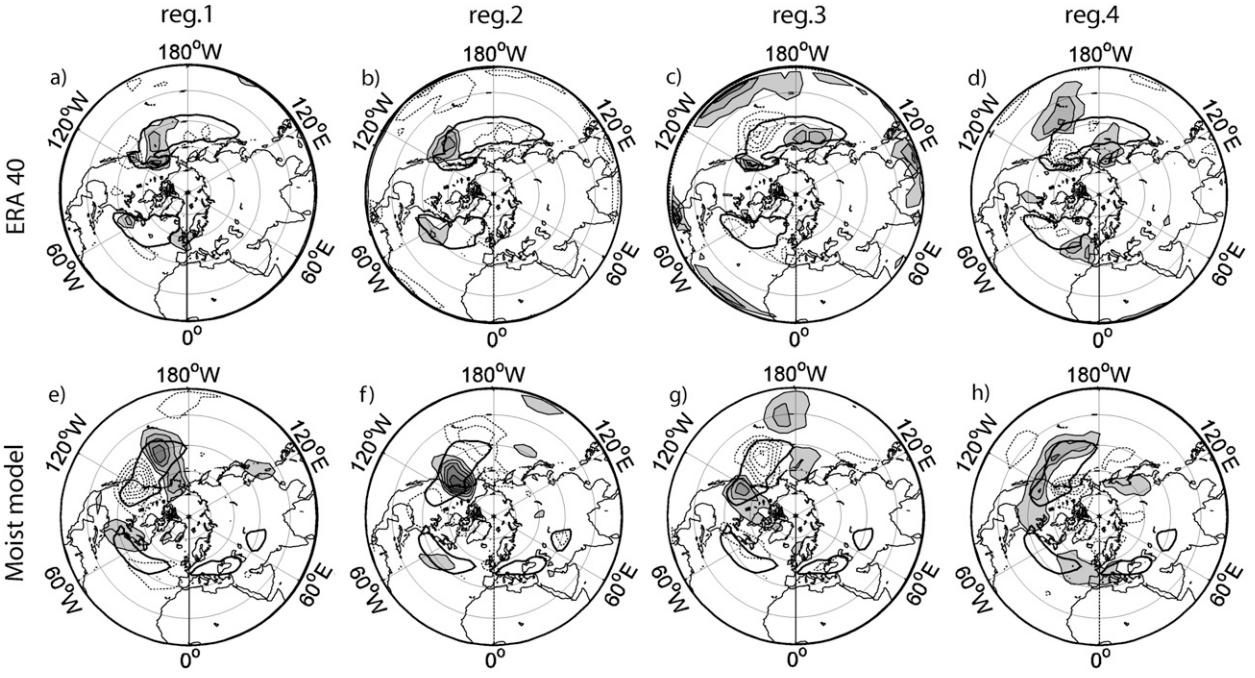

FIG. 9. Composite of the large-scale precipitation rate anomalies associated with the regimes presented in Fig. 4 for (a)–(d) ERA-40 and (e)–(h) the moist model. Contours are every 0.4 mm day^{-1}, the zero contours are not plotted for clarity, gray shading is positive values, and dashed contours are negative values. Thick contours represent climatological large-scale precipitation rates of 3 mm day^{-1} for ERA-40 and 6 mm day^{-1} for the moist model.

4. Conclusions

We have developed a moist quasigeostrophic model to study the effect of moist processes on storm tracks and the low-frequency atmospheric variability. The moist model exhibits different characteristics than the dry model. The intensity of the Northern Hemisphere mean jet is reduced in its central and northern part and slightly enhanced in its southern portion. The jet maximum is too weak in the moist model compared to ERA-40 even if the zonal wind bias with ERA-40 is smaller than for the dry model (due to the southward enhancement). Eddies break more cyclonically in the moist model, which is more consistent with ERA-40, although the mean occurrence is still not high enough. Too much AWB occurrence occurs in both models, which is consistent with a general bias of QG models, as explained in Rivière (2009). The WB differences seem mainly responsible for the mean zonal-wind differences between the models and ERA-40 but only partly for those between the moist and the dry model. In particular, the decrease of the jet maxima in the moist model compared to the dry model is due to the latent heating term induced by the synoptic variability, which overcompensates for the change in the forcing term. The storm track is usually located slightly to the north of the jets and the underlying precipitation leads to a warming there, thereby decreasing the meridional temperature gradient and consequently the jet through the thermal wind balance. The consequence is a slight decrease in storm-track eddy activity for the moist model.

The North Pacific storm track is relatively well reproduced in the models, although it is located too far north (as for the jet) and associated with too few CWB occurrences and too many AWB events. The North Atlantic storm track is very poorly simulated, with weaker high-frequency variability than in ERA-40, and it is not properly separated from the North Pacific storm track. The low-frequency variability of the moist model is not very different from the dry model in the Pacific but usually improves in the North Atlantic, consistent with a better representation of WB properties. In general, the differences in the WB characteristics of each weather regime are consistent with the jet latitudinal displacements through eddy–mean flow interactions. The precipitation anomalies associated with each regime indicate that the moist model is able to reproduce realistic precipitation differences associated with flow anomalies, despite its mean flow biases, which consist of too strong precipitation rates and an eastward displacement of the mean North Pacific precipitation zone.

The moist model includes an additional physical component to the dry model, without unrealistically disturbing its general characteristics. The moist model improves some biases of the dry model (a southward intensification of the jet, better WB characteristics, and associated improved

weather regime patterns in the North Atlantic), although the changes are usually much weaker than the differences from ERA-40. However, this type of simple model does not pretend to properly simulate all aspects of the climate system, but at least many aspects of the moist storm tracks are fairly reproduced. Therefore, despite its mean biases, it could be used for sensitivity experiments. For example, different variabilities of the present-day climate (intraseasonal variations, interannual oscillations, or mean trends) could be studied. To this end, composite climatic conditions can be used to calculate the corresponding forcing terms. If the moist QG model simulates properly the climatic changes related to the different periods considered, then this can be used to examine how the differences in PV, moisture and mean temperature forcing (and combinations of these) change the midlatitude climate. In particular, the question of how changes in water vapor or temperature in warmer or colder conditions modify the climate of the midlatitudes could be considered.

Acknowledgments. This work has been partially funded by Agence Nationale de la Recherche, under contract ANR-06-JCJC-133-01. Guillaume Lapeyre acknowledges funding from Fondation MAIF on a grant REVAEE.

APPENDIX A

Derivation of the QG PV Equations Including Diabatic Processes

To obtain the QG PV equation, one first needs to approximate temperature using the hydrostatic balance Eq. (6) and replacing Φ with $f_0\psi$ (see MM93; Mak 1991). Then the temperature equation (without temperature relaxation and forcing) becomes

$$\frac{f_0 p_{ij}}{R_{\text{air}}\Delta p}\left(\frac{\partial}{\partial t} + \mathbf{u}_{ij}\cdot\nabla\right)(\psi_i - \psi_j) = -\left(\frac{\partial T}{\partial p} - \frac{R_{\text{air}}\,T}{C_{\text{pd}}\,p_{ij}}\right)\omega_{ij} + \frac{L_{\text{vap}}}{C_{\text{pd}}}\,\mathcal{P}_{ij}, \qquad \text{(A1)}$$

with $ij = 12$ or 23 denoting the upper or lower layer. The static stability, entering as a factor of ω_{ij} in the first term of the rhs of the equation, is assumed to be constant in QG formalism. We then use $R_{ij} = (\Delta p/f_0)\sqrt{(R_{\text{air}}/p_{ij})(\partial T/\partial p - R_{\text{air}}T/C_{\text{pd}}p)}$, so that the equation becomes

$$R_{ij}^{-2}\left(\frac{\partial}{\partial t} + \mathbf{u}_{ij}\cdot\nabla\right)(\psi_i - \psi_j) = -\frac{f_0}{\Delta p}\,\omega_{ij} + \frac{L_{\text{vap}}R_{\text{air}}\Delta p}{C_{\text{pd}}f_0 p_{ij}}R_{ij}^{-2}\mathcal{P}_{ij}. \qquad \text{(A2)}$$

To obtain Eq. (3), we replace $\Delta p/p_{ij}$ with $\log(p_i/p_j)$. Note that we use dry static stability for both dry and moist models since it determines the Rossby radii of deformation, which we want equal in both models for proper comparison.

APPENDIX B

Derivation of the QG Vertical Velocity Equation

The QG temperature equation allows us to express the vertical velocity in QG as

$$\omega_{ij} = -\frac{\Delta p}{f_0}\sin\phi\left\{R_{ij}^{-2}\left[\frac{\partial(\psi_i - \psi_j)}{\partial t} + J(\psi_{ij}, \psi_i - \psi_j) - S_i^{\psi} + S_j^{\psi} + \frac{\psi_i - \psi_j}{\tau}\right] - \mathcal{L}_{ij}\right\}, \qquad \text{(B1)}$$

where $\mathcal{L}_{ij} = \mathcal{L}_1$ for $ij = 12$ and $\mathcal{L}_{ij} = -\mathcal{L}_3$ for $ij = 23$; $S_{i/j}^m$ is the forcing term in terms of streamfunction field obtained inverting $S_{i/j}$ as a PV source. Also, $\sin\phi$ takes into account the change of sign of f between the two hemispheres without causing discontinuity at the equator.

To obtain the vertical velocity in QG, we first invert the PV tendency Eqs. (1) to obtain streamfunction tendency equations $\partial_t\psi_i$ at each vertical level.

REFERENCES

Alexander, M. A., C. Deser, and M. S. Timlin, 1999: The reemergence of SST anomalies in the North Pacific Ocean. *J. Climate,* **12,** 2419–2433.

Andrews, D. G., and M. E. McIntyre, 1976: Planetary waves in horizontal and vertical shear: The generalized Eliassen–Palm relation and the mean zonal acceleration. *J. Atmos. Sci.,* **33,** 2031–2048.

Benedict, J. J., S. Lee, and S. B. Feldstein, 2004: Synoptic view of the North Atlantic Oscillation. *J. Atmos. Sci.,* **61,** 121–144.

Branstator, G., 1995: Organization of storm track anomalies by recurring low-frequency circulation anomalies. *J. Atmos. Sci.,* **52,** 207–226.

Chang, E. K. M., 2006: An idealized nonlinear model of the Northern Hemisphere winter storm tracks. *J. Atmos. Sci.,* **63,** 1818–1839.

——, and I. Orlanski, 1993: On the dynamics of a storm track. *J. Atmos. Sci.,* **50,** 999–1015.

——, S. Lee, and K. L. Swanson, 2002: Storm track dynamics. *J. Climate,* **15,** 2163–2183.

Corti, S., A. Giannini, S. Tibaldi, and F. Molteni, 1997: Patterns of low-frequency variability in a three-level quasi-geostrophic model. *Climate Dyn.,* **13,** 883–904.

——, F. Molteni, and T. N. Palmer, 1999: Signature of recent climate change in frequencies of natural atmospheric circulation regimes. *Nature,* **398,** 799–802.

D'Andrea, F., and R. Vautard, 2001: Extratropical low-frequency variability as a low-dimensional problem. I: A simplified model. *Quart. J. Roy. Meteor. Soc.,* **127,** 1357–1374.

Frierson, D. M. W., I. M. Held, and P. Zurita-Gotor, 2006: A gray-radiation aquaplanet moist GCM. Part I: Static stability and eddy scale. *J. Atmos. Sci.,* **63,** 2548–2566.

——, ——, and ——, 2007: A gray-radiation aquaplanet moist GCM. Part II: Energy transports in altered climates. *J. Atmos. Sci.,* **64,** 1680–1693.

Held, I. M., and B. J. Soden, 2006: Robust responses of the hydrological cycle to global warming. *J. Climate,* **19,** 5686–5699.

Hoskins, B. J., and P. J. Valdes, 1990: On the existence of storm-tracks. *J. Atmos. Sci.,* **47,** 1854–1864.

Kimoto, M., and M. Ghil, 1993: Multiple flow regimes in the Northern Hemisphere winter. Part I: Methodology and hemispheric regimes. *J. Atmos. Sci.,* **50,** 2625–2644.

Laîné, A., M. Kageyama, D. Salas-Mélia, G. Ramstein, S. Planton, S. Denvil, and S. Tyteca, 2009: An energetics study of wintertime Northern Hemisphere storm tracks under $4 \times CO_2$ conditions in two ocean–atmosphere coupled models. *J. Climate,* **22,** 819–839.

Lapeyre, G., and I. M. Held, 2004: The role of moisture in the dynamics and energetics of turbulent baroclinic eddies. *J. Atmos. Sci.,* **61,** 1693–1710.

Lau, N.-C., 1988: Variability of the observed midlatitude storm tracks in relation to low-frequency changes in the circulation pattern. *J. Atmos. Sci.,* **45,** 2718–2743.

Lott, F., 1999: Alleviation of stationary biases in a GCM through a mountain drag parameterization scheme and a simple representation of mountain lift forces. *Mon. Wea. Rev.,* **127,** 788–801.

Mak, M., 1991: Influences of the earth's sphericity in the quasi-geostrophic theory. *J. Meteor. Soc. Japan,* **69,** 497–510.

Marshall, J., and F. Molteni, 1993: Toward a dynamical understanding of planetary-scale flow regimes. *J. Atmos. Sci.,* **50,** 1792–1818.

Martius, O., C. Schwierz, and H. C. Davies, 2007: Breaking waves at the tropopause in the wintertime Northern Hemisphere: Climatological analyses of the orientation and the theoretical LC1/2 classification. *J. Atmos. Sci.,* **64,** 2576–2592.

Michelangeli, P.-A., R. Vautard, and B. Legras, 1995: Weather regimes: Recurrence and quasi stationarity. *J. Atmos. Sci.,* **52,** 1237–1256.

Nakamura, H., T. Sampe, Y. Tanimoto, and A. Shimpo, 2004: Observed associations among storm tracks, jet streams and midlatitude oceanic fronts. *Earth's Climate: The Ocean–Atmosphere Interaction, Geophys. Monogr.,* Vol. 147, Amer. Geophys. Union, 329–346.

Opsteegh, J. D., R. J. Haarsma, F. M. Selten, and A. Kattenberg, 1998: ECBILT: A dynamic alternative to mixed boundary conditions in ocean models. *Tellus,* **50A,** 348–367.

Orlanski, I., 2003: Bifurcation in eddy life cycles: Implications for storm track variability. *J. Atmos. Sci.,* **60,** 993–1023.

——, 2005: A new look at the Pacific storm track variability: Sensitivity to tropical SSTs and to upstream seeding. *J. Atmos. Sci.,* **62,** 1367–1390.

Rivière, G., 2009: Effect of latitudinal variations in low-level baroclinicity on eddy life cycles and upper-tropospheric wave-breaking processes. *J. Atmos. Sci.,* **66,** 1569–1592.

——, and I. Orlanski, 2007: Characteristics of the Atlantic storm-track eddy activity and its relation with the North Atlantic Oscillation. *J. Atmos. Sci.,* **64,** 241–266.

——, A. Laîné, G. Lapeyre, D. Salas-Mélia, and M. Kageyama, 2010: Links between Rossby wave breaking and the North Atlantic Oscillation–Arctic Oscillation in present-day and Last Glacial Maximum climate simulations. *J. Climate,* **23,** 2987–3008.

Schneider, T., and P. A. O'Gorman, 2008: Moist convection and the thermal stratification of the extratropical troposphere. *J. Atmos. Sci.,* **65,** 3571–3583.

Soden, B. J., and I. M. Held, 2006: An assessment of climate feedbacks in coupled ocean–atmosphere models. *J. Climate,* **19,** 3354–3360.

Solomon, A., 2006: Impact of latent heat release on polar climate. *Geophys. Res. Lett.,* **33,** L07716, doi:10.1029/2005GL025607.

Solomon, S., D. Qin, M. Manning, M. Marquis, K. Averyt, M. M. B. Tignor, H. L. Miller Jr., and Z. Chen, Eds., 2007: *Climate Change 2007: The Physical Science Basis*. Cambridge University Press, 996 pp.

Son, S.-W., and S. Lee, 2005: The response of westerly jets to thermal driving in a primitive equation model. *J. Atmos. Sci.,* **62,** 3741–3757.

Strong, C., and G. Magnusdottir, 2008: Tropospheric Rossby wave breaking and the NAO/NAM. *J. Atmos. Sci.,* **65,** 2861–2876.

Thorncroft, C. D., B. J. Hoskins, and M. E. McIntyre, 1993: Two paradigms of baroclinic-wave life-cycle behaviour. *Quart. J. Roy. Meteor. Soc.,* **119,** 17–55.

Vautard, R., and B. Legras, 1988: On the source of midlatitude low-frequency variability. Part II: Nonlinear equilibration of weather regimes. *J. Atmos. Sci.,* **45,** 2845–2867.

Wernli, H., and M. Sprenger, 2007: Identification and ERA-15 climatology of potential vorticity streamers and cutoffs near the extratropical tropopause. *J. Atmos. Sci.,* **64,** 1569–1586.

Zhang, J., 1995: Effects of latent heating on midlatitude atmospheric general circulation. Ph.D. thesis, Princeton University, 194 pp.